nature genetics

Mutations in *KCNH1* and *ATP6V1B2* cause Zimmermann-Laband syndrome

Fanny Kortüm[1,21], Viviana Caputo[2,21], Christiane K Bauer[3,21], Lorenzo Stella[4], Andrea Ciolfi[5], Malik Alawi[6–8], Gianfranco Bocchinfuso[4], Elisabetta Flex[5], Stefano Paolacci[2,5], Maria Lisa Dentici[9], Paola Grammatico[10], Georg Christoph Korenke[11], Vincenzo Leuzzi[12], David Mowat[13,14], Lal D V Nair[15], Thi Tuyet Mai Nguyen[16], Patrick Thierry[17], Susan M White[18,19], Bruno Dallapiccola[9], Antonio Pizzuti[2], Philippe M Campeau[20], Marco Tartaglia[5,9,22] & Kerstin Kutsche[1,22]

Zimmermann-Laband syndrome (ZLS) is a developmental disorder characterized by facial dysmorphism with gingival enlargement, intellectual disability, hypoplasia or aplasia of nails and terminal phalanges, and hypertrichosis[1–4]. We report that heterozygous missense mutations in *KCNH1* account for a considerable proportion of ZLS. *KCNH1* encodes the voltage-gated K^+ channel Eag1 ($K_v10.1$). Patch-clamp recordings showed strong negative shifts in voltage-dependent activation for all but one KCNH1 channel mutant (Gly469Arg). Coexpression of Gly469Arg with wild-type KCNH1 resulted in heterotetrameric channels with reduced conductance at positive potentials but pronounced conductance at negative potentials. These data support a gain-of-function effect for all ZLS-associated KCNH1 mutants. We also identified a recurrent *de novo* missense change in *ATP6V1B2*, encoding the B2 subunit of the multimeric vacuolar H^+ ATPase, in two individuals with ZLS. Structural analysis predicts a perturbing effect of the mutation on complex assembly. Our findings demonstrate that *KCNH1* mutations cause ZLS and document genetic heterogeneity for this disorder.

The main clinical characteristics of ZLS (MIM 135500) are gingival enlargement, a bulbous soft nose, thick floppy ears, nail aplasia or hypoplasia, hypertrichosis, joint hyperextensibility, hepato(spleno)megaly, and intellectual disability with or without epilepsy. Most cases are sporadic, suggesting autosomal dominant inheritance with *de novo* mutations[5]. Two translocations sharing a 3p14.3 breakpoint region, including *CACNA2D3* and *WNT5A*, have been associated with ZLS[6–8]. *CACNA2D3*, encoding the auxiliary α2δ-3 subunit of voltage-gated Ca^{2+} channels, was found to be disrupted in one individual[7]. However, no additional mutations in *CACNA2D3* or *WNT5A* have been identified[6,9] nor has any other causative gene for this disease.

We performed whole-exome sequencing on five unrelated subjects with core features of ZLS (subjects 1, 4, 5, 7 and 8; **Figs. 1** and **2**) and the healthy parents of four of them (Online Methods). Subjects 5, 7 and 8 had been reported previously as having typical ZLS[5,7,9]. We processed the whole-exome sequencing data to identify genes shared among probands having functionally relevant variants (new, clinically associated, or of low or unknown frequency), taking into account X-linked, autosomal recessive and autosomal dominant inheritance models (**Supplementary Table 1**). We identified one to seven putatively *de novo* variants in the four trios (**Supplementary Table 2**). *KCNH1* had *de novo* variants in subjects 1 (c.1399A>G, p.Ile467Val), 4 (c.1405G>A, p.Gly469Arg) and 5 (c.1054C>G, p.Leu352Val) (NM_002238.3; NP_002229.1) (**Fig. 1a** and **Supplementary Table 1**), and subjects 7 and 8 had an identical *de novo* missense variant in *ATP6V1B2* (c.1454G>C, p.Arg485Pro) (NM_001693.3; NP_001684.2) (**Fig. 1a** and **Supplementary Table 1**). We validated these variants by Sanger sequencing, and parental genotyping confirmed their *de novo* origin. Sequencing confirmed occurrence of the variants in all tissues available for subjects 4 and 5 (mutated *KCNH1*

[1]Institute of Human Genetics, University Medical Center Hamburg-Eppendorf, Hamburg, Germany. [2]Dipartimento di Medicina Sperimentale, Università La Sapienza, Rome, Italy. [3]Department of Cellular and Integrative Physiology, University Medical Center Hamburg-Eppendorf, Hamburg, Germany. [4]Dipartimento di Scienze e Tecnologie Chimiche, Università 'Tor Vergata', Rome, Italy. [5]Dipartimento di Ematologia, Oncologia e Medicina Molecolare, Istituto Superiore di Sanità, Rome, Italy. [6]University Medical Center Hamburg-Eppendorf, Bioinformatics Service Facility, Hamburg, Germany. [7]Center for Bioinformatics, University of Hamburg, Hamburg, Germany. [8]Heinrich Pette Institute, Leibniz Institute for Experimental Virology, Virus Genomics, Hamburg, Germany. [9]Ospedale Pediatrico Bambino Gesù–Istituto di Ricovero e Cura a Carattere Scientifico, Rome, Italy. [10]Dipartimento di Medicina Molecolare, Università La Sapienza, Ospedale San Camillo-Forlanini, Rome, Italy. [11]Zentrum für Kinder- und Jugendmedizin, Neuropädiatrie, Klinikum Oldenburg, Oldenburg, Germany. [12]Dipartimento di Pediatria e Neuropsichiatria Infantile, Università La Sapienza, Rome, Italy. [13]Department of Medical Genetics, Sydney Children's Hospital, Sydney, New South Wales, Australia. [14]School of Women's and Children's Health, University of New South Wales Medicine, University of New South Wales, Sydney, New South Wales, Australia. [15]Department of Pediatrics, Saveetha Medical College and Hospital, Saveetha University, Chennai, India. [16]Sainte-Justine Hospital Research Center, University of Montreal, Montreal, Quebec, Canada. [17]Service de Pédiatrie, Centre Hospitalier Intercommunal de la Haute-Saône, Vesoul, France. [18]Victorian Clinical Genetics Services, Murdoch Childrens Research Institute, Royal Children's Hospital, Melbourne, Victoria, Australia. [19]Department of Paediatrics, University of Melbourne, Melbourne, Victoria, Australia. [20]Department of Pediatrics, Sainte-Justine Hospital, University of Montreal, Montreal, Quebec, Canada. [21]These authors contributed equally to this work. [22]These authors jointly supervised this work. Correspondence should be addressed to K.K. (kkutsche@uke.de) or M.T. (marco.tartaglia@iss.it).

Received 29 October 2014; accepted 23 March 2015; published online 27 April 2015; doi:10.1038/ng.3282

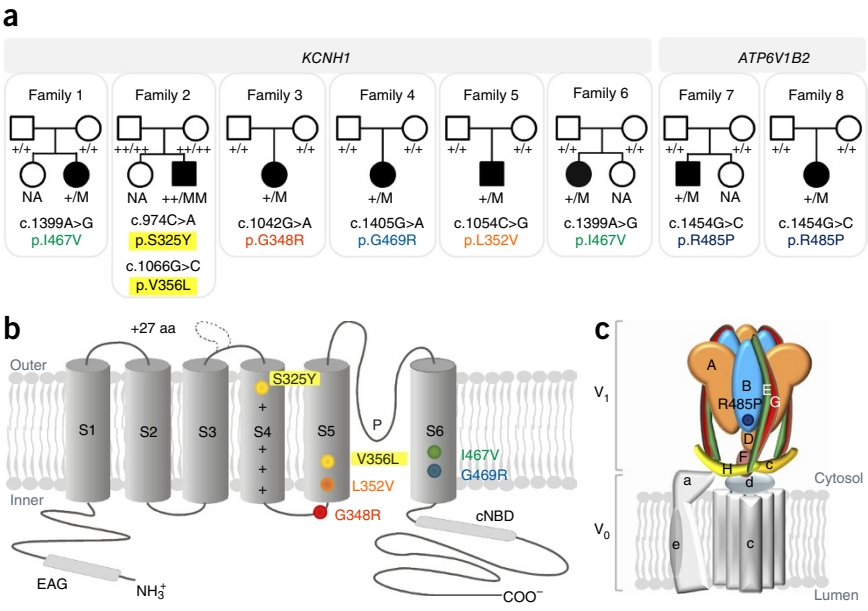

Figure 1 Heterozygous missense mutations in *KCNH1* and *ATP6V1B2* in individuals with ZLS. (**a**) Pedigrees and segregation analysis of disease-associated *KCNH1* and *ATP6V1B2* variants. *KCNH1* mutations are described according to the shorter isoform (NM_002238.3; NP_002229.1). NA, not analyzed; +, wild-type allele; M, mutant allele; MM, two mutations in *cis*. (**b**) Schematic of the KCNH1 channel showing the location of the residues affected in individuals with ZLS (colored dots). The S1–S4 segments act as voltage-sensor domains, and the assembly of four subunits is required to form a functional channel (not shown). cNBD, cyclic nucleotide-binding domain; EAG, EAG domain; P, pore region. (**c**) Schematic view of the subunit structure of the V-ATPase. The catalytic V_1 complex consists of the A, B, C, D, E, F, G and H subunits. The V_0 domain is membrane embedded and is composed of a characteristic C-ring structure with which the a, d and e subunits are associated. Arg485 is highlighted by a blue dot. The colors of the mutated residues (indicated by dots in **b** and **c**) correspond to the colors of the *KCNH1* and *ATP6V1B2* missense mutations in **a**.

alleles) and subject 7 (*ATP6V1B2* mutation) (**Supplementary Fig. 1**). We screened 19 additional individuals exhibiting clinical features fitting ZLS for mutations in each gene. We found that two *KCNH1* missense changes—the already-identified c.1399A>G (p.Ile467Val)

Figure 2 Clinical features of ZLS-affected individuals with a *KCNH1* or *ATP6V1B2* mutation. (**a**–**d**) Facial phenotype of subjects (S) with *KCNH1* mutation: S1 (**a**), S3 (**b**), S4 (**c**) and S5 (**d**). Note the central incisor in S3 and gingival enlargement in S3 and S5. For a detailed description, see **Supplementary Table 5**. (**e**,**g**) S1 shows anonychia of the right great toe and hypoplastic nails of all other right toes and fingers of left hand. (**f**,**h**) Radiographs of S1 showing hypoplastic terminal phalanges of the thumb, great toe and third to fifth toes and aplastic terminal phalanx of the second toe. (**i**,**j**) S2 shows aplastic nails of the thumb and first to third toes and hypoplastic nails of all other fingers and toes. (**k**,**l**) S4 shows absence of hypoplasia or aplasia of nails and terminal phalanges. (**m**,**n**) S5 shows anonychia of the thumbs and great toes and nail hypoplasia of the right fifth finger and right second to fifth toes. (**o**) S6 shows anonychia of the left great toe and hyponychia of all other toes. (**p**–**r**) Facial appearance of subjects with *ATP6V1B2* mutation: shown are S7 as a neonate (**p**) and at age 12 years (**q**) and S8 (**r**). (**s**,**t**) Gingival enlargement in S7 (**s**) and S8 (**t**). (**u**–**x**) Anonychia of the hands and feet in S7 and S8. (**u**,**v**) S7 shows aplastic terminal phalanges of the second and fifth fingers on the left hand, the fifth finger on the right hand and all toes except the first. (**w**,**x**) S8 shows shortened second to fourth fingers, except the third finger on the right hand, and toes. Hypertrichosis occurs in S7 (**u**,**v**) and S8 (**y**). Consent for the publication of photographs was obtained for all individuals. The images in **d** and **t** are reproduced from ref. 5. Copyright © 2013 Elsevier Masson SAS. All rights reserved.

substitution and c.1042G>A (p.Gly348Arg)—occurred as *de novo* mutations in subjects 6 and 3, respectively (**Fig. 1a**). We documented two heterozygous variants (c.974C>A, p.Ser325Tyr; c.1066G>C, p.Val356Leu) in subject 2 (**Fig. 1a**); both variants were *de novo* and were demonstrated to be present in *cis* (**Supplementary Fig. 1**). None of the *de novo* changes were annotated in the dbSNP138, 1000 Genomes Project, Exome Variant Server and ExAC databases. *KCNH1* and *ATP6V1B2* are predicted to be intolerant to functional genetic variation[10,11]. All mutations affected residues invariantly observed among vertebrates (**Supplementary Fig. 2**) and were predicted to have a damaging impact on protein function (**Supplementary Table 3**). Overall, the identification of a *KCNH1* or *ATP6V1B2* mutation in 8 of the 24 patients analyzed indicates further genetic heterogeneity in ZLS.

KCNH1 encodes the Eag1 (K_v10.1) channel, a member of the EAG (ether-à-go-go) family of voltage-gated K^+ channels[12]. The KCNH1 channel activates at relatively depolarized potentials and conducts a mainly non-inactivating, delayed-rectifier K^+ current[13]. KCNH1 subunits exhibit a typical K_v membrane topology, with six transmembrane domains (S1–S6) and a pore-lining loop between S5 and S6 (**Fig. 1b**). The affected amino acid residues were located in the voltage-sensing S4 helix (Ser325), the S4–S5 linker (Gly348), and the S5 (Leu352 and Val356) and S6 (Ile467 and Gly469) segments (**Fig. 1b**). We explored the structural impact of four of the six mutations by using a homology model for the S5 and S6 helices (**Fig. 3**). In the closed state, the Gly469 residues of two KCNH1 monomers are located close to each other, whereas they are farther apart in the open structure. As the p.Gly469Arg change inserts four cationic residues close to each other in the closed state of the homotetramer, this substitution is predicted to impair tetramer formation or favor the open state with a lower conductance due to the presence of cationic residues close to the channel pore (**Fig. 3a**–c). A similar effect is expected in heterotetramers of wild-type and mutant subunits. The Ile467, Leu352 and Val356 residues form a tight hydrophobic cluster in the open structure, which rearranges in the closed conformation (**Fig. 3a**,**b**,**d**). Perturbations of these residues are predicted to affect the closed-open transition. Consistently, mutations in *KCNH2* affecting the residues corresponding

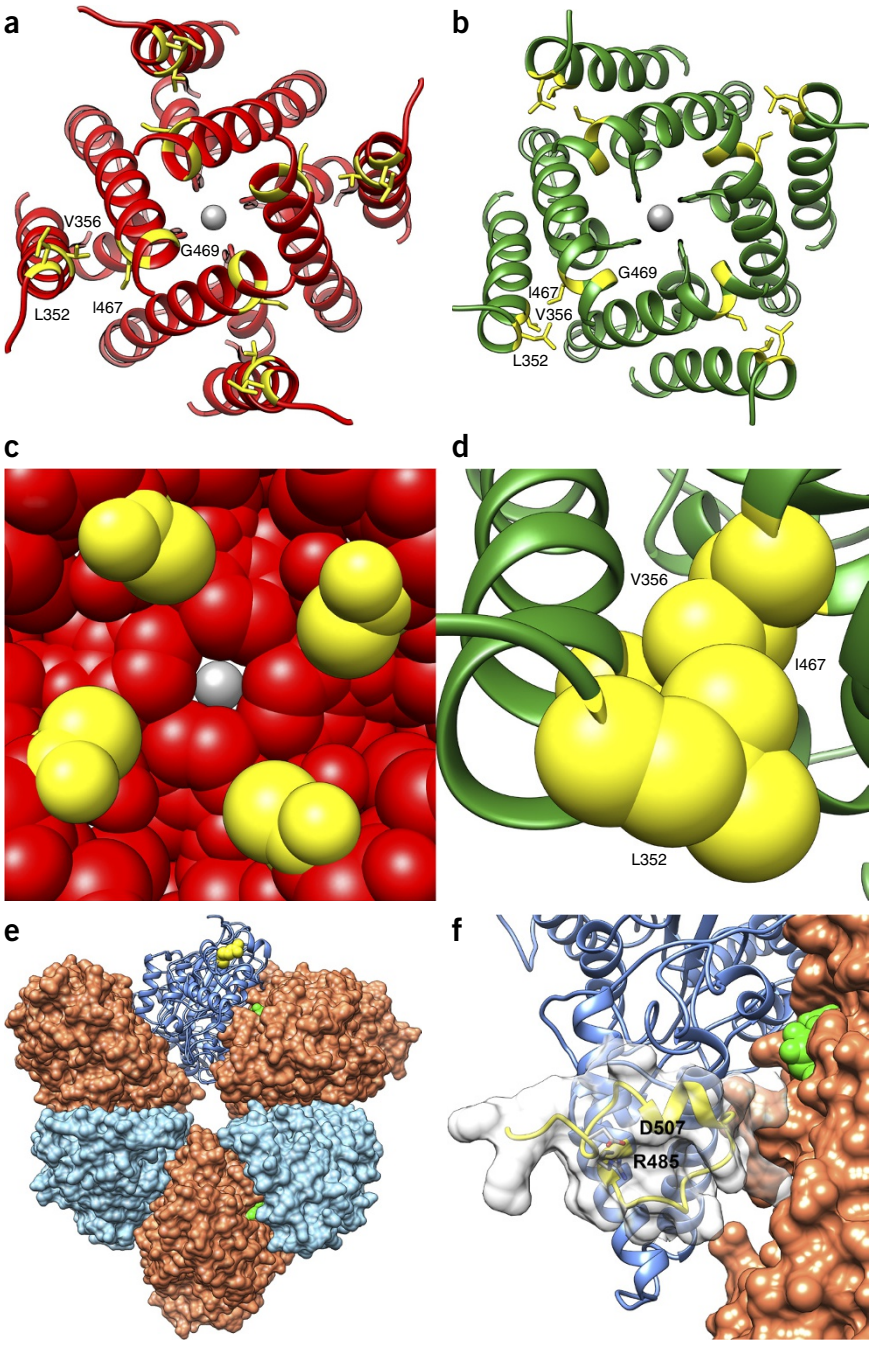

Figure 3 Structural impact of ZLS-associated *KCNH1* and *ATP6V1B2* mutations. (**a**) Model of helices S5 and S6 of KCNH1 in their closed state (viewed from the intracellular side of the membrane). Affected residues (yellow) and K^+ (gray sphere) are shown. (**b**) Model of helices S5 and S6 of KCNH1 in their open state. The color code is as in **a**. (**c**) Enlargement of the pore-closing region in the closed state. Atoms are shown as spheres to illustrate the steric hindrance of this region, which would hardly accommodate a larger charged residue, such as arginine, at position 469. (**d**) Enlargement of the hydrophobic cluster formed by Leu352, Val356 and Ile467 (side chains shown in sphere representation) in the open state. (**e**) Homology model of the B subunit of the human V-ATPase (ribbon representation) in the context of the A_3B_3 hexamer of the *E. hirae* ATPase (surface representation, with A subunits colored in salmon and B subunits colored in light blue). The complex is shown as seen from the membrane surface. One of the B subunits was substituted by the homology model of the B subunit of the human V-ATPase (ribbon representation). ATP analogs are shown in green, and Arg485 is represented in yellow. (**f**) Enlargement of the A-B interface. Arg485 and Asp507 are shown in stick representation. The C-terminal segment of the B subunit predicted to be destabilized by the p.Arg485Pro substitution is represented in yellow. The space-filling model of residues 485–511 is also shown, as a semitransparent white surface.

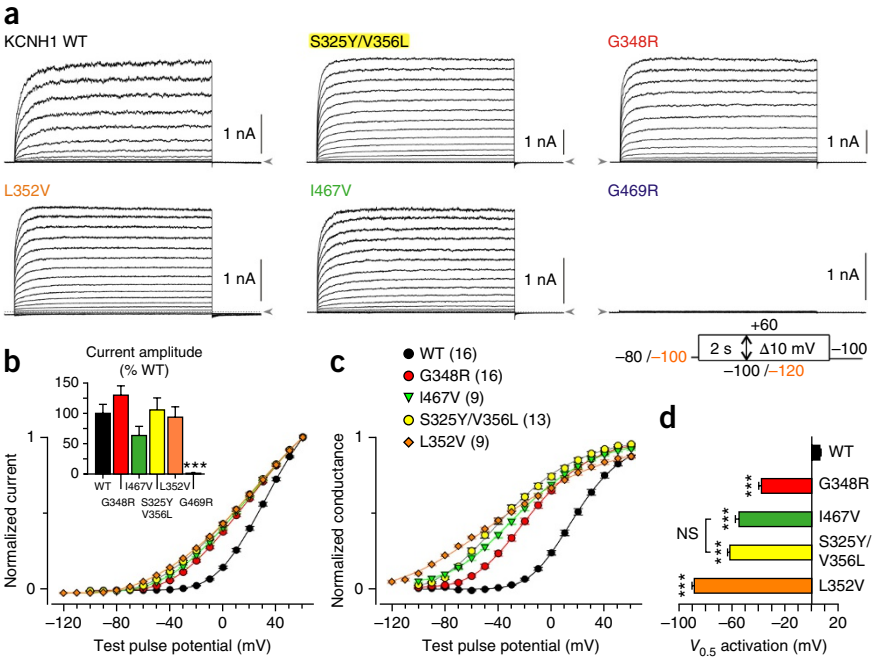

Figure 4 Voltage-dependent activation of human wild-type (WT) and mutant KCNH1 channels expressed in CHO cells. (**a**) Families of whole-cell currents elicited with 2-s variable test pulses as indicated in the pulse protocol shown at the right below the current traces. For the Leu352Val mutant, a more negative holding potential of −100 mV and test pulses starting from −120 mV were used. Expression of the Gly469Arg mutant did not result in recordings of voltage-dependent K^+ currents ($n = 22$). Zero current is indicated by dashed lines and arrowheads. (**b**) Mean (±s.e.m.) KCNH1 current amplitudes as a function of the test pulse potential. Current amplitudes were normalized to the maximum amplitude recorded at +60 mV. Data points were connected by straight lines. The inset shows current amplitudes at +40 mV normalized to the mean current for the wild-type channel. (***$P < 0.001$, significantly different from wild type) (**c**) Mean (±s.e.m.) normalized whole-cell conductance as a function of the test pulse potential. Lines represent fourth-order Boltzmann functions fitted to the data points. Numbers of experiments are shown in parentheses. (**d**) Mean (+s.e.m.) values of the potential of half-maximal KCNH1 channel activation ($V_{0.5\ activation}$), derived from fits to permeability data considering the Goldman-Hodgkin-Katz current equation. One-way ANOVA with *post-hoc* Bonferroni *t* testing yielded significant (***$P < 0.001$) differences for all combinations except the one indicated (NS, not significant). The parameters of the fits to whole-cell conductance and channel activation data are summarized in **Supplementary Table 4**. (**b**–**d**) Represent analyses from the same experiments.

to Ile467 and Gly469 in KCNH1 have been demonstrated to favor the open state of the encoded ERG1 channel[14,15].

We assessed the functional consequences of the ZLS-associated *KCNH1* mutations by patch-clamp experiments on CHO cells expressing wild-type or mutant KCNH1 channels. We recorded outward-rectifying, essentially non-inactivating currents for wild-type KCNH1 and the Gly348Arg, Leu352Val, Ile467Val and Ser325Tyr/Val356Leu KCNH1 mutants, demonstrating expression of functional channels (**Fig. 4a**). The current amplitudes of the mutants did not differ significantly ($P = 0.127$, one-way ANOVA) from the amplitudes of wild-type KCNH1; all mutant channels, however, exhibited a remarkable shift in the activation threshold to more negative potentials (**Fig. 4b**), producing dramatic increases in whole-cell K^+ conductance in the negative-potential range (**Fig. 4c**). This effect resulted from strong leftward shifts in the voltage dependence of channel activation in comparison to wild-type KCNH1 (**Fig. 4d** and **Supplementary Table 4**). We confirmed these calculated differences in the voltage for half-maximal channel activation by instantaneous tail current measurements (**Supplementary Fig. 3**). In comparison to wild-type channels, the mutants exhibited accelerated channel activation and slower deactivation (**Supplementary Fig. 4**). Notably, the altered voltage dependence of the double mutant, Ser325Tyr/Val356Leu, resulted from additive effects produced by each individual substitution (**Supplementary Fig. 5** and **Supplementary Table 4**). Coexpression of wild-type KCNH1 and the Gly348Arg mutant, which exhibited the smallest shift in voltage dependence, resulted in currents with an intermediate activation threshold and voltage values for half-maximal conductance still 20 mV more negative than those measured for wild-type channels (**Fig. 5a–c** and **Supplementary Table 4**). These data indicate that the p.Gly348Arg, p.Leu352Val, p.Ile467Val and p.[Ser325Tyr; Val356Leu] substitutions have a gain-of-function effect. In contrast, the Gly469Arg mutant failed to produce voltage-dependent outward currents (**Fig. 4a**,**b**).

We next coexpressed wild-type and Gly469Arg KCNH1 channels in CHO cells. Although the resulting current profile overlapped that observed for the wild-type homotetramer, an additional, smaller component with half-maximal conductance at about −45 mV and a small leakage K^+ current evident at negative potentials was recorded (**Fig. 5d–f** and **Supplementary Table 4**). The mean current amplitude at +40 mV corresponded to 69.9% of the respective value for the wild-type channel (s.e.m. of 10.9%; $P = 0.12$) (**Fig. 5e**, inset). As KCNH1 expression levels varied considerably across CHO cells, we used *Xenopus laevis* oocytes and found that coexpression of Gly469Arg and wild-type KCNH1 resulted in significantly smaller current amplitudes at +40 mV than expression of homomeric wild-type channels ($P < 0.001$; **Supplementary Fig. 6**). Similar to in CHO cells, we recorded no depolarization-activated currents when homomeric Gly469Arg channels were expressed. These data document a dominant action of the Gly469Arg mutant over the wild-type channel, with reduced K^+ conductance of the heterotetrameric channels at depolarizing potentials but with pronounced conductance at negative potentials, similar to our findings for the other ZLS-causing KCNH1 mutants. Together, our data show a gain-of-function effect for all disease-associated KCNH1 mutants, similar to the recently identified *KCNH5* mutation encoding p.Arg327His in the EAG2 channel in a patient with severe epileptic encephalopathy[16,17].

We found *ATP6V1B2* to be mutated in two ZLS-affected individuals. *ATP6V1B2* encodes the B2 subunit of the vacuolar H^+ ATPase (V-ATPase), a multisubunit enzyme that mediates acidification in organelles by pumping protons against an electrochemical gradient[18,19]. V-ATPases comprise a cytoplasmic catalytic V_1 subcomplex and a membrane-embedded V_0 subcomplex (**Fig. 1c**). To explore the structural impact of the p.Arg485Pro amino acid change, we generated a homology model of the B2 subunit and inserted it into the crystallographic structure of the A_3B_3 hexamer of the *Enterococcus hirae* ATPase[20]. As Arg485 is far from the ATP-binding site, the

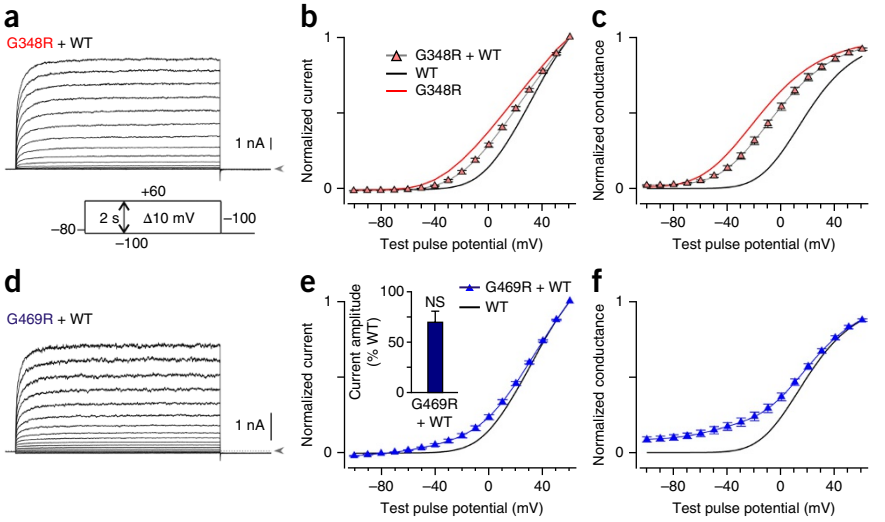

Figure 5 Voltage-dependent activation of KCNH1 K^+ currents resulting from coexpression of wild-type KCNH1 with mutant KCNH1 channel subunits in CHO cells using a 1:1 cDNA ratio. (**a**) Representative whole-cell currents resulting from Gly348Arg + wild type coexpression. (**b**,**c**) Voltage dependence of normalized Gly348Arg + wild type current amplitudes (**b**) and whole-cell conductance (**c**). Means (±s.e.m.) of six experiments are shown. The gray line in **c** represents a fit of the data points using equation (2) (Online Methods). Corresponding data for homomeric Gly348Arg and wild-type channels are shown for comparison as red and black lines, respectively. (**d**) Representative whole-cell currents recorded from cells expressing Gly469Arg + wild type. Zero current is indicated by a dashed line and arrowhead. (**e**,**f**) Voltage dependence of normalized current amplitudes (**e**) and whole-cell conductance (**f**) for Gly469Arg + wild type. Means (±s.e.m.) of 14 experiments are shown. The blue line in **f** represents a fit of the data points using equation (3) (Online Methods). Corresponding data for homomeric wild-type channels are shown for comparison as black lines, and the inset in **e** illustrates the mean current amplitude at +40 mV normalized to the mean current for the wild-type channel. Fit parameters are summarized in **Supplementary Table 4**.

p.Arg485Pro substitution is not expected to affect the affinity of the protein for its substrate (**Fig. 3e**). Arg485 is however located in an α-helical segment that is predicted to be disrupted by substitution to proline. Moreover, the salt bridge with Asp507 is lost in the mutant (**Fig. 3f**). Overall, the arginine-to-proline substitution is predicted to perturb intersubunit interactions within the V_1 subcomplex by destabilizing the C-terminal segment of the B subunit, which is part of the A-B interface and interacts with the E subunit[21].

In this work, we have provided genetic, structural and functional evidence supporting the dysregulation of KCNH1 in ZLS pathogenesis. *KCNH1* is predominantly expressed in the brain[22]; however, its role in cell cycle control and proliferation is documented in multiple cell lineages, including human bone marrow–derived mesenchymal stem cells[23–27]. *Kcnh1*-null mice develop normally and display normal brain morphology and behavior, aside from mild hyperactivity[28], indicating that, in contrast to hyperactive KCNH1 channels, null alleles of *KCNH1* are likely to be tolerated. Consistent with the identification of dominant missense mutations in *KCNJ8* and *ABCC9*, encoding the ATP-sensitive potassium (K_{ATP}) channel Kir6.1 and its regulatory subunit SUR2, in Cantú syndrome[29–32], our findings demonstrate that a balance of K^+ channel activities is not only critical for neurons but also for other cells and tissues during development.

KCNH1 channels contribute to resting membrane potentials in the vicinity of −40 mV[12], which are thus close to the activation threshold of L-type voltage-gated Ca^{2+} channels[33]. All ZLS-causing *KCNH1* mutations induce considerable K^+ conductance at negative potentials. Stabilization of the membrane potential in a more negative voltage range impedes opening of both voltage-gated Na^+ and Ca^{2+} channels. Thus, functional blockage of these channels could be a secondary effect of the *KCNH1* mutations, which may explain the

Table 1 Genetic and clinical characteristics of the individuals with *KCNH1* or *ATP6V1B2* mutation identified in this study

Subject	1	2[a]	3[a]	4	5[b]	6	7[a]	8[b]
Gene	*KCNH1*	*KCNH1*	*KCNH1*	*KCNH1*	*KCNH1*	*KCNH1*	*ATP6V1B2*	*ATP6V1B2*
Mutation[c]	c.1399A>G p.Ile467Val	c.974C>A p.Ser325Tyr c.1066G>C p.Val356Leu	c.1042G>A p.Gly348Arg	c.1405G>A p.Gly469Arg	c.1054C>G p.Leu352Val	c.1399A>G p.Ile467Val	c.1454G>C p.Arg485Pro	c.1454G>C p.Arg485Pro
Inheritance	*De novo*	Both *de novo*	*De novo*	*De novo*	*De novo*	*De novo*	*De novo*	*De novo*
Sex	F	M	F	F	M	F	M	F
ID	+	+	+	+	+	+	+	+
Seizures	+	+	+	+	+	+	–	–
Hearing loss	–	–	–	NA	NA	+	+	–
Coarse face	+	+	+	+	+	+	+	+
Gingival enlargement	+	+	+	+	+	–	+	+
Aplastic or hypoplastic nails	+	+	+	–	+	+	+	+
Aplastic or hypoplastic terminal phalanges	+	NA	+	–	+	+	+	+
Scoliosis	+	+	+	+	+	–	+	ND
Hypertrichosis	+	–	–	+	+	–	+	+

+, present; –, absent; F, female; ID, intellectual disability; M, male; NA, not analyzed; ND, not documented.
[a]Published in ref. 9 (subject 2 is patient 9 from Table 2, subject 3 is patient 7 from Table 1 and subject 7 is patient 6 from Table 1). [b]Published in ref. 5 (subject 5 is patient 2, and subject 8 is patient 1). [c]*KCNH1* nucleotide and amino acid changes are reported with respect to the short transcript variant 2 (NM_002238.3; NP_002229.1); *ATP6V1B2* nucleotide and amino acid changes are reported with respect to the reference sequences (NM_001693.3; NP_001684.2).

similarity of the gingival enlargement in ZLS-affected subjects to what is observed in some individuals treated with the Na^+ channel blocker phenytoin[34,35] or the Ca^{2+} channel blocker nifedipine[36].

ZLS belongs to a group of syndromes characterized by considerable clinical overlap and genetic heterogeneity, such as Temple-Baraitser syndrome (TBS; MIM 611816)[37], dominant deafness-onychodystrophy syndrome (DDOD; MIM 124480)[38] and autosomal recessive deafness, onychodystrophy, osteodystrophy, mental retardation, seizures syndrome (DOORS; MIM 220500)[39]. Intellectual disability, epilepsy, deafness, hypoplasia or aplasia of nails and/or terminal phalanges, and gingival enlargement vary between the different disorders as well as within each condition. The common clinical features in the individuals positive for *KCNH1* and *ATP6V1B2* mutations reported here include craniofacial dysmorphism, gingival enlargement (preceding any anticonvulsant use), mild to severe intellectual disability, and aplastic or hypoplastic nails and terminal phalanges (**Fig. 2**, **Table 1** and **Supplementary Table 5**). Seizures and/or epilepsy were present in all six subjects with *KCNH1* mutations but absent in the two individuals with the *ATP6V1B2* mutation, who exhibited coarser facial features. Other clinical features, such as hearing loss and hypertrichosis, were variably present in the eight individuals with a *KCNH1* or *ATP6V1B2* mutation (**Table 1** and **Supplementary Table 5**). Recently, *de novo KCNH1* gain-of-function mutations have been reported in individuals with TBS[40], further indicating that both TBS and ZLS belong to a phenotypic continuum that needs to be characterized in the future.

Our genetic data also indicate that alterations of the V-ATPase B2 subunit account for a small proportion of ZLS. ATP6V1B2 is ubiquitously expressed and is the only B subunit isoform expressed in osteoclasts, suggesting an involvement in regulating bone reabsorption[41–43]. Recently, a heterozygous nonsense *ATP6V1B2* mutation, c.1516C>T (p.Arg506*), has been reported in DDOD[44]. Consistent with partial clinical overlap, the ZLS- and DDOD-causing *ATP6V1B2* mutations affect the same protein region, which participates in V_1 subcomplex assembly. Truncation of the same segment of ATP6V1B1 disrupts V_1 assembly and impairs ATPase function[21]. Although defective V-ATPase function has been associated with the p.Arg506* alteration[44] and a qualitatively similar effect for the p.Arg485Pro substitution cannot be ruled out, further studies are required to understand the precise functional consequences of these alterations.

In conclusion, we identified *KCNH1* and *ATP6V1B2* as disease-associated genes for ZLS. So far, only hypothetical functional links exist between the two encoded proteins. Both the V-ATPase and KCNH1 have been shown to regulate neurotransmitter release and are important for synaptic transmission[45,46]. The V-ATPase serves in the acidification of intracellular organelles[47], and effective proton pumping requires the movement of a counterion. Initial data indicate that K^+ could act as the counterion[48,49]. Although no cation channel has yet emerged as a candidate counterion transporter, rapid internalization of plasma membrane–localized KCNH1 and its sorting to lysosomes[50] provide a first clue of the function of KCNH1 in lysosomal conductive pathways. Alternatively, altered acidification of intracellular compartments may lead to disturbances in cellular transport processes in general and to perturbed regulation of KCNH1 trafficking in particular[50,51].

URLs. 1000 Genomes Project, http://www.1000genomes.org/; database for nonsynonymous SNPs' functional predictions (dbNSFP), https://sites.google.com/site/jpopgen/dbNSFP; dbSNP, http://www.ncbi.nlm.nih.gov/SNP/; ExAC database, http://exac.broadinstitute.org/; Exome Variant Server, National Heart, Lung, and Blood Institute (NHLBI) Grand Opportunity (GO) Exome Sequencing Project (ESP), http://evs.gs.washington.edu/EVS/; NCBI Gene database, http://www.ncbi.nlm.nih.gov/gene/; Online Mendelian Inheritance in Man (OMIM), http://www.omim.org; Protein Data Bank (PDB), http://www.rcsb.org/pdb/home/home.do; Picard tool, http://picard.sourceforge.net/.

METHODS

Methods and any associated references are available in the online version of the paper.

Accession codes. Reference sequences for *KCNH1* are available from NCBI under accessions NM_172362.2 and NP_758872.1 for transcript variant 1 (longer isoform) and under accessions NM_002238.3 and NP_002229.1 for transcript variant 2 (shorter isoform). The NCBI reference sequences for *ATP6V1B2* are NM_001693.3 and NP_001684.2.

Note: Any Supplementary Information and Source Data files are available in the online version of the paper.

ACKNOWLEDGMENTS

We are grateful to the patients and their families who contributed to this study. We thank I. Jantke, S. Cecchetti and S. Venanzi for skillful technical assistance, T. Kock for site-directed mutagenesis, A. Hasse for CHO cell transfection and injection, R. Bähring, J.M. Schröder and E. Neumann for help with the oocyte experiments, P. Meinecke for discussing clinical phenotypes and A. Podolska for help with *ATP6V1B2* sequencing. G.B., L.S. and M.T. acknowledge CINECA for computational resources (whole-exome sequencing data and structural analyses). The KCNH1/heag1 clone was kindly provided by S.H. Heinemann (Friedrich Schiller University Jena). This work was supported by grants from the Deutsche Forschungsgemeinschaft (KO 4576/1-1 to F.K. and KU 1240/5-1 to K.K.), Istituto Superiore di Sanità (Ricerca Corrente 2013 to M.T.), Ministero della Salute (Ricerca Finalizzata RF-2010-2312766 to B.D.) and Ospedale Pediatrico Bambino Gesù (Gene-Rare to B.D.).

AUTHOR CONTRIBUTIONS

F.K. performed whole-exome sequencing data analysis and validation, molecular screening and genotyping and wrote the manuscript. V.C. performed whole-exome sequencing data analysis and validation and wrote the manuscript. C.K.B. contributed the electrophysiological studies and wrote the manuscript. L.S. and G.B. performed the homology modeling and structural analysis. A.C. and M.A. contributed to the whole-exome sequencing data processing and analysis. E.F., S.P., M.L.D. and T.T.M.N. carried out the molecular screening and/or genotyping. P.G., G.C.K., V.L., D.M., L.D.V.N., P.T., S.M.W., B.D. and A.P. recruited and clinically characterized the study subjects and collected the biological samples. P.M.C. performed whole-exome sequencing data analysis, validation and genotyping. M.T. and K.K. conceived the project, analyzed and interpreted the data, and wrote the manuscript. All authors contributed to the final manuscript.

COMPETING FINANCIAL INTERESTS

The authors declare no competing financial interests.

1. Laband, P.F., Habib, G. & Humphreys, G.S. Hereditary gingival fibromatosis. Report of an affected family with associated splenomegaly and skeletal and soft-tissue abnormalities. *Oral Surg. Oral Med. Oral Pathol.* **17**, 339–351 (1964).
2. Alavandar, G. Elephantiasis gingivae. Report of an affected family with associated hepatomegaly, soft tissue and skeletal abnormalities. *J. All India Dent. Assoc.* **37**, 349–353 (1965).
3. Chacon-Camacho, O.F., Vazquez, J. & Zenteno, J.C. Expanding the phenotype of gingival fibromatosis–mental retardation–hypertrichosis (Zimmermann-Laband) syndrome. *Am. J. Med. Genet.* **155A**, 1716–1720 (2011).
4. Dávalos, I.P. *et al.* Zimmermann-Laband syndrome: further clinical delineation. *Genet. Couns.* **16**, 283–290 (2005).
5. Castori, M. *et al.* Clinical and genetic study of two patients with Zimmermann-Laband syndrome and literature review. *Eur. J. Med. Genet.* **56**, 570–576 (2013).
6. Abo-Dalo, B. *et al.* Extensive molecular genetic analysis of the 3p14.3 region in patients with Zimmermann-Laband syndrome. *Am. J. Med. Genet.* **143A**, 2668–2674 (2007).

7. Kim, H.G. *et al.* Candidate loci for Zimmermann-Laband syndrome at 3p14.3. *Am. J. Med. Genet.* **143A**, 107–111 (2007).
8. Stefanova, M. *et al.* Zimmermann-Laband syndrome associated with a balanced reciprocal translocation t(3;8)(p21.2;q24.3) in mother and daughter: molecular cytogenetic characterization of the breakpoint regions. *Am. J. Med. Genet. A.* **117A**, 289–294 (2003).
9. Abo-Dalo, B. *et al.* No mutation in genes of the WNT signaling pathway in patients with Zimmermann-Laband syndrome. *Clin. Dysmorphol.* **17**, 181–185 (2008).
10. Petrovski, S. *et al.* Genic intolerance to functional variation and the interpretation of personal genomes. *PLoS Genet.* **9**, e1003709 (2013).
11. Samocha, K.E. *et al.* A framework for the interpretation of *de novo* mutation in human disease. *Nat. Genet.* **46**, 944–950 (2014).
12. Bauer, C.K. & Schwarz, J.R. Physiology of EAG K^+ channels. *J. Membr. Biol.* **182**, 1–15 (2001).
13. Garg, V., Sachse, F.B. & Sanguinetti, M.C. Tuning of EAG K^+ channel inactivation: molecular determinants of amplification by mutations and a small molecule. *J. Gen. Physiol.* **140**, 307–324 (2012).
14. Thouta, S. *et al.* Proline scan of the HERG channel S6 helix reveals the location of the intracellular pore gate. *Biophys. J.* **106**, 1057–1069 (2014).
15. Wynia-Smith, S.L., Gillian-Daniel, A.L., Satyshur, K.A. & Robertson, G.A. hERG gating microdomains defined by S6 mutagenesis and molecular modeling. *J. Gen. Physiol.* **132**, 507–520 (2008).
16. Veeramah, K.R. *et al.* Exome sequencing reveals new causal mutations in children with epileptic encephalopathies. *Epilepsia* **54**, 1270–1281 (2013).
17. Yang, Y. *et al.* Multistate structural modeling and voltage-clamp analysis of epilepsy/autism mutation K_v10.2-R327H demonstrate the role of this residue in stabilizing the channel closed state. *J. Neurosci.* **33**, 16586–16593 (2013).
18. Forgac, M. Vacuolar ATPases: rotary proton pumps in physiology and pathophysiology. *Nat. Rev. Mol. Cell Biol.* **8**, 917–929 (2007).
19. Marshansky, V., Rubinstein, J.L. & Gruber, G. Eukaryotic V-ATPase: novel structural findings and functional insights. *Biochim. Biophys. Acta* **1837**, 857–879 (2014).
20. Arai, S. *et al.* Rotation mechanism of *Enterococcus hirae* V1-ATPase based on asymmetric crystal structures. *Nature* **493**, 703–707 (2013).
21. Fuster, D.G., Zhang, J., Xie, X.S. & Moe, O.W. The vacuolar-ATPase B1 subunit in distal tubular acidosis: novel mutations and mechanisms for dysfunction. *Kidney Int.* **73**, 1151–1158 (2008).
22. Martin, S. *et al.* Eag1 potassium channel immunohistochemistry in the CNS of adult rat and selected regions of human brain. *Neuroscience* **155**, 833–844 (2008).
23. Hemmerlein, B. *et al.* Overexpression of Eag1 potassium channels in clinical tumours. *Mol. Cancer* **5**, 41 (2006).
24. Pardo, L.A. & Stühmer, W. The roles of K^+ channels in cancer. *Nat. Rev. Cancer* **14**, 39–48 (2014).
25. Ouadid-Ahidouch, H. & Ahidouch, A. K^+ channel expression in human breast cancer cells: involvement in cell cycle regulation and carcinogenesis. *J. Membr. Biol.* **221**, 1–6 (2008).
26. Weber, C. *et al.* Silencing the activity and proliferative properties of the human Eagl potassium channel by RNA interference. *J. Biol. Chem.* **281**, 13030–13037 (2006).
27. Zhang, Y.Y. *et al.* BK_{Ca} and hEag1 channels regulate cell proliferation and differentiation in human bone marrow–derived mesenchymal stem cells. *J. Cell. Physiol.* **229**, 202–212 (2014).
28. Ufartes, R. *et al.* Behavioural and functional characterization of K_v10.1 (Eag1) knockout mice. *Hum. Mol. Genet.* **22**, 2247–2262 (2013).
29. Harakalova, M. *et al.* Dominant missense mutations in *ABCC9* cause Cantú syndrome. *Nat. Genet.* **44**, 793–796 (2012).
30. van Bon, B.W. *et al.* Cantú syndrome is caused by mutations in *ABCC9*. *Am. J. Hum. Genet.* **90**, 1094–1101 (2012).
31. Brownstein, C.A. *et al.* Mutation of *KCNJ8* in a patient with Cantú syndrome with unique vascular abnormalities—support for the role of K_{ATP} channels in this condition. *Eur. J. Med. Genet.* **56**, 678–682 (2013).
32. Cooper, P.E. *et al.* Cantú syndrome resulting from activating mutation in the *KCNJ8* gene. *Hum. Mutat.* **35**, 809–813 (2014).
33. Lipscombe, D., Helton, T.D. & Xu, W. L-type calcium channels: the low down. *J. Neurophysiol.* **92**, 2633–2641 (2004).
34. Corrêa, J.D. *et al.* Phenytoin-induced gingival overgrowth: a review of the molecular, immune, and inflammatory features. *ISRN Dent.* **2011**, 497850 (2011).
35. Mantegazza, M. *et al.* Voltage-gated sodium channels as therapeutic targets in epilepsy and other neurological disorders. *Lancet Neurol.* **9**, 413–424 (2010).
36. Wynn, R.L. Calcium channel blockers and gingival hyperplasia—an update. *Gen. Dent.* **57**, 105–107 (2009).
37. Jacquinet, A. *et al.* Temple-Baraitser syndrome: a rare and possibly unrecognized condition. *Am. J. Med. Genet.* **152A**, 2322–2326 (2010).
38. White, S.M. & Fahey, M. Report of a further family with dominant deafness-onychodystrophy (DDOD) syndrome. *Am. J. Med. Genet.* **155A**, 2512–2515 (2011).
39. Campeau, P.M. & Hennekam, R.C. DOORS syndrome: phenotype, genotype and comparison with Coffin-Siris syndrome. *Am. J. Med. Genet.* **166C**, 327–332 (2014).
40. Simons, C. *et al.* Mutations in the voltage-gated potassium channel gene *KCNH1* cause Temple-Baraitser syndrome and epilepsy. *Nat. Genet.* **47**, 73–77 (2015).
41. Nelson, R.D. *et al.* Selectively amplified expression of an isoform of the vacuolar H^+-ATPase 56-kilodalton subunit in renal intercalated cells. *Proc. Natl. Acad. Sci. USA* **89**, 3541–3545 (1992).
42. Puopolo, K. *et al.* Differential expression of the "B" subunit of the vacuolar H^+-ATPase in bovine tissues. *J. Biol. Chem.* **267**, 3696–3706 (1992).
43. van Hille, B. *et al.* Heterogeneity of vacuolar H^+-ATPase: differential expression of two human subunit B isoforms. *Biochem. J.* **303**, 191–198 (1994).
44. Yuan, Y. *et al. De novo* mutation in *ATP6V1B2* impairs lysosome acidification and causes dominant deafness-onychodystrophy syndrome. *Cell Res.* **24**, 1370–1373 (2014).
45. Mortensen, L.S. *et al.* K_V10.1 opposes activity-dependent increase in Ca^{2+} influx into the presynaptic terminal of the parallel fibre–Purkinje cell synapse. *J. Physiol. (Lond.)* **593**, 181–196 (2015).
46. Poëa-Guyon, S. *et al.* The V-ATPase membrane domain is a sensor of granular pH that controls the exocytotic machinery. *J. Cell Biol.* **203**, 283–298 (2013).
47. Mindell, J.A. Lysosomal acidification mechanisms. *Annu. Rev. Physiol.* **74**, 69–86 (2012).
48. Steinberg, B.E. *et al.* A cation counterflux supports lysosomal acidification. *J. Cell Biol.* **189**, 1171–1186 (2010).
49. Van Dyke, R.W. Acidification of rat liver lysosomes: quantitation and comparison with endosomes. *Am. J. Physiol.* **265**, C901–C917 (1993).
50. Kohl, T., Lörinczi, E., Pardo, L.A. & Stühmer, W. Rapid internalization of the oncogenic K^+ channel K_V10.1. *PLoS ONE* **6**, e26329 (2011).
51. Ninkovic, M. *et al.* Physical and functional interaction of K_V10.1 with Rabaptin-5 impacts ion channel trafficking. *FEBS Lett.* **586**, 3077–3084 (2012).

ONLINE METHODS

Subjects. In this study, we included 24 individuals with a phenotype fitting ZLS or suggestive of the disorder. They were clinically assessed by experienced clinical geneticists and/or neurologists. Of these, five patients had previously been reported[5,9]. Clinical features are summarized in **Table 1** and described in detail in **Supplementary Table 5**. Informed consent for DNA storage and genetic analyses was obtained from the parents or legal guardians of all subjects, and genetic studies were approved by all institutional review boards of the participating institutions. Permission to publish photographs was given for all subjects shown in **Figure 2**.

Whole-exome sequencing and data analysis. Targeted enrichment and massively parallel sequencing were performed on genomic DNA extracted from circulating leukocytes. Enrichment of the whole exome was performed using the Nextera Enrichment kit (62 Mb) (Illumina) for subjects 1 and 7 and their parents, SureSelect AllExonV4 (51 M) (Agilent Technologies) for subject 4 and her parents, and NimbleGen SeqCap EZ Library v.3.0 (64 Mb) (Roche) for subjects 5 and 8 and the parents of subject 8, according to the manufacturers' protocols. Each captured library was then loaded onto the HiSeq 2000 platform (Illumina). Raw image files were processed by CASAVA software 1.7 or 1.8 (Illumina) for base calling, with default parameters, and the sequences of each individual were generated as 90-bp reads. Reads were aligned to the human reference genome (UCSC GRCh37/hg19) using the Burrows-Wheeler Aligner (BWA v.0.7.10)[52]. Low-quality bases were trimmed from 3′ ends by applying the parameter '-q 15' when invoking BWA. Alignments belonging to the same sample were merged using the Picard tool. Presumed PCR duplicates were removed using Picard's MarkDuplicates. The Genome Analysis Toolkit (GATK 3.2)[53] was used for realignment of sequences encompassing indels and for base quality recalibration.

SNPs and small indels were identified by means of the GATK HaplotypeCaller and UnifiedGenotyper algorithms[53], applying the following quality filters: variants with quality >100 and quality-by-depth score >1.5 were retained; variants below these thresholds or resulting from four or more reads having ambiguous mapping (this number being greater than 10% of all aligned reads) were discarded. Only variants called by both algorithms were considered. Variants were filtered against available public databases (dbSNP138, 1000 Genomes Project, Exome Variant Server and ExAC; only clinically associated variants and variants of unknown frequency or with MAF <0.1% were retained) and in-house databases. SnpEff toolbox (v3.6)[54] was used to predict the functional impact of variants, which were filtered to retain only functionally relevant variants (i.e., missense, nonsense and coding indel variants and intronic variants located from −5 to +5 with respect to an exon-intron junction). Functional annotation of variants was performed using SnpEff v3.6 and dbNSFP2.5 (refs. 54,55).

Variant validation and mutation analysis. Sequence validation and segregation analyses for all the candidate variants, as well as mutation scanning of the entire *KCNH1* (NM_172362.2 and NM_002238.3) and *ATP6V1B2* (NM_001693.3) coding sequences, were performed by Sanger sequencing. Primer pairs designed to amplify the coding exons of the two genes and their intron boundaries (*KCNH1*: NC_000001.11, 210,678,315–211,134,115, complement; *ATP6V1B2*: NC_000008.11, 20,197,193–20,221,696) and PCR conditions are available upon request. Amplicons were directly sequenced using the ABI BigDye Terminator Sequencing kit (Applied Biosystems) and an automated capillary sequencer (ABI 3500, Applied Biosystems). Sequence electropherograms were analyzed using Sequence Pilot software (JSI Medical Systems) and Sequencing Analysis Software v.5.4 (Applied Biosystems). Genotyping was carried out with the PowerPlex ESX16 System kit (Promega) and the AmpFl STR SGM plus kit (Applied Biosystems) to confirm paternity and maternity. The effects of predicted amino acid substitutions were assessed with Radial Support Vector Machine (RadialSVM)[55] and Combined Annotation-Dependent Depletion (CADD)[56].

Haplotype determination. Exon 7 of *KCNH1* and adjacent intronic sequences were amplified from the genomic DNA of subject 2. The PCR product was cloned into the pCR2.1 TOPO TA Cloning Vector (Invitrogen), and the resulting vectors were transformed into *Escherichia coli*. Sixteen individual *Escherichia coli* clones were picked and subjected to colony PCR and Sanger sequencing.

Structural analyses. We generated homology models of helices S5 and S6 of the K^+ voltage-gated channel, subfamily H member 1 (KCNH1) and the B subunit (isoform 2) of the human V-ATPase, ATP6V1B2, on the basis of the available crystallographic structures of homologous proteins.

In the case of KCNH1, the sequence identity with available experimental structures was relatively low (15–30%), and no suitable templates were available for the whole S1–S6 sequence. Comparison of these structures, however, documented that even proteins with very low homology in sequence were characterized by an extremely similar conformation and relative arrangement of the membrane-embedded segments corresponding to helix S5 (residues 350–370 in KCNH1), the pore-forming segment and helix S6 (residues 424–471). The only major difference between structures was represented by the presence of a kink in the S6 helices containing a conserved PVP motif, which is absent in the KCNH1 sequence[14]. The high similarity of the structures for the S5 and S6 helices in proteins lacking the PVP motif supports the validity of obtaining a homology model for this region, where most of the identified disease-causing alterations were located (hereafter, residue positions are with reference to the shorter KCNH1 isoform). Two models of the S5 helix–S6 helix region (residues 350–471), referring to the open and closed channel states, were obtained by using the SWISS-MODEL server[57]. For the open state, the K_vAP voltage-dependent K^+ channel from *Aeropyrum pernix* (Protein Data Bank (PDB) 1ORQ; 23% identity) served as a template for both the homology modeling and the quaternary structure assembly. For the closed state, the structure of the K^+ complex of the NaK channel (PDB 2AHZ; 29% identity) was used as the template, which was assembled on the basis of the structure of the voltage-gated K^+ channel of *Listeria monocytogenes* in its closed state (PDB 4H33). All these templates lack the kink-inducing PVP motif.

For ATP6V1B2, a homology model was generated by using the I-Tasser server[58] and templates with sequence identities ranging from 55 to 59% (PDB 3GQB, 3VR6, 2C61, 3VR4 and 3A5C). The model was fitted on the structure of the A_3B_3 complex determined crystallographically for the *E. hirae* ATPase bound to a non-hydrolyzable ATP analog (PDB 3VR3).

Molecular graphics were developed with UCSF Chimera software[59].

Site-directed mutagenesis. *KCNH1* single mutations encoding p.Ile467Val, p.Ser325Tyr, p.Gly348Arg, p.Leu352Val, p.Val356Leu and p.Gly469Arg and the two mutations encoding p.[Ser325Tyr; Val356Leu] were introduced into *KCNH1* cDNA with the QuikChange Site-Directed Mutagenesis kit (Agilent Technologies). All constructs were sequenced for integrity.

Heterologous KCNH1 expression in CHO cells and *Xenopus* oocytes. Chinese hamster ovary (CHO) cells were originally obtained from the American Type Culture Collection (ATCC). Cells were not recently tested for mycoplasma. CHO cells were transfected with cDNA for wild-type or mutant human KCNH1 (hEAG1, isoform 1) and cDNA encoding EGFP-N1 (Clontech) using Lipofectamine 2000 (Invitrogen) as described previously[60]. The final concentration of *KCNH1* cDNA cloned into the pcDNA3 vector (Invitrogen) was 200 ng/ml. For wild-type and Gly469Arg coexpression, 200 ng/ml of each plasmid was used. For coexpression experiments of wild-type and Gly348Arg channels, CHO cells were microinjected using a Transjector 5246 (Eppendorf) with equal amounts of both *KCNH1* plasmids (17 ng/µl) together with EGFP-N1 plasmid as described previously[60].

Xenopus oocytes were collected under anesthesia (Tricain; 1.2 g/l), and the follicular tissue was removed by treatment with collagenase A (Roche). Before and after injection with cRNA, oocytes were kept at 18 °C in medium containing 75 mM NaCl, 5 mM sodium pyruvate, 2 mM KCl, 2 mM $CaCl_2$, 1 mM $MgCl_2$ and 5 mM HEPES; pH adjusted to 7.5 with NaOH and supplemented with 50 mg/l gentamicin. *Xenopus* oocytes were injected with cRNA encoding either wild-type KCNH1 channel (5 ng/50 nl) or the KCNH1 mutant Gly469Arg (5 ng/50 nl) using a Nanoliter 2000 microinjector (World Precision Instruments). In the coexpression experiments, the 50-nl injection volume contained 5 ng of each *KCNH1* cRNA. Oocytes were used for experiments 2 d after injection. All experimental procedures were performed in accordance with the national guidelines for the care and

doi:10.1038/ng.3282

use of research animals and were approved by the Institutional Animal Care and Use Committee of Hamburg (Germany).

Electrophysiology. Patch-clamp experiments were performed 5–30 h after CHO cell transfection or microinjection in the conventional whole-cell configuration of the patch-clamp technique. The external Ringer solution contained 140 mM NaCl, 5 mM KCl, 0.8 mM $MgCl_2$, 1 mM $CaCl_2$, 5 mM glucose and 10 mM HEPES; pH adjusted to 7.4 with NaOH. The pipette solution contained 140 mM KCl, 2 mM $MgCl_2$, 1 mM $CaCl_2$, 2.5 mM EGTA and 10 mM HEPES; pH adjusted to 7.3 with KOH. Patch pipettes had resistances of 1.5 to 3 MΩ. The access resistance ranged from 1.8 to 5 MΩ, and series resistance was compensated for by at least 70%. Signals were compensated for both fast and slow capacity transients, low-pass filtered at 10 and 3 kHz, and digitized at a sample interval of 0.2–1 ms. Data were not corrected for the liquid junction potential error of about 4 mV, and no leak subtraction was performed.

An EPC-9 patch-clamp amplifier was used in combination with PULSE stimulation and data acquisition software (HEKA Elektronik). The standard activation protocol consisted of variable 2-s test pulses every 10 s from a holding potential of −80 mV. A more negative holding potential of −100 mV was necessary for the Leu352Val KCNH1 channel owing to its considerable conductance at −80 mV. All test pulses were followed by a constant hyperpolarizing pulse to −100 mV. Additional pulse protocols are depicted in the figures. The experiments were performed at room temperature (20–21 °C).

Xenopus oocyte currents were recorded with the two-electrode voltage-clamp technique using a Turbo TEC 03 amplifier (npi electronic) and PATCHMASTER acquisition software (HEKA Elektronik). The external solution contained 91 mM NaCl, 5 mM KCl, 1 mM $MgCl_2$, 1 mM $CaCl_2$ and 5 mM HEPES; pH adjusted to 7.4 with NaOH. Pipettes were filled with 3 M KCl solution. Experiments were performed at room temperature.

Data analysis. Patch-clamp data processing was performed with PulseFit 8.65 (HEKA), Excel (Microsoft) and Sigmaplot 11.0 (Systat Software). Current amplitudes were determined as mean values during the last period of the 2-s test pulses or as maximal current amplitude for slightly inactivating current traces. The manifestation of KCNH1 channel inactivation at the most positive potentials was variable for all channel constructs. Experiments with pronounced inactivation at a test pulse potential of +60 mV were not included in the data analysis. Because of high variability in current amplitudes for each channel construct, the current amplitudes from individual experiments were normalized to the maximum current amplitude recorded during the test pulse to +60 mV. Conductance-voltage (*G*-*V*) relationships were determined on the basis of the equation

$$G = I_{\mathrm{norm}} / (V - V_{\mathrm{rev}}) \quad (1)$$

where I_{norm} is the normalized current amplitude at the test pulse potential V and V_{rev} is the current reversal potential, determined from the resting membrane potential measured in the current-clamp mode or interpolated from the current reversal potential derived from deactivation protocols. Only for the experiments with wild-type KCNH1 channels, a fixed value of −70 mV was used. *G*-*V* relationships were analyzed with a fourth-order Boltzmann function of the form

$$G/G_{\mathrm{max}} = 1/((1 + \exp(-(V - V')/s))^4) \quad (2)$$

where G/G_{max} is the normalized whole-cell conductance at a test pulse potential V. The voltage dependence is defined by V' (6.25% of the maximal conductance) and the slope factor s. The $V_{0.5\,\mathrm{conductance}}$ values in **Supplementary Table 4** are the potentials where the above function had a value of 0.5.

The conductance data resulting from coexpression of wild-type and Gly469Arg channel constructs were not well fitted by the fourth-order Boltzmann function, indicating more than one channel population with differences in the voltage dependence of activation. These data were fitted by the sum of a fourth-order Boltzmann function (to allow direct comparison with wild-type channel properties), a first-order Boltzmann function and a leak conductance component

$$G/G_{\mathrm{max}} = a/((1 + \exp(-(V - V')/s))^4) + b/(1 + \exp(-(V - V_{0.5})/k)) + c \quad (3)$$

where a, b and c indicate the relative contributions of the three conductance components, with $V_{0.5}$ as the potential of half-maximal conductance and k as the slope factor for component b.

The voltage dependence of KCNH1 channel activation (or the relative open probability of the channels) was assessed by describing normalized K^+ current values according to a simplified Goldman-Hodgkin-Katz current equation[61,62] to account for unequal K^+ concentrations in the external and internal solutions

$$I_{\mathrm{K}} = P_{\mathrm{K}} V((1 - \exp(-(V - V_{\mathrm{rev}})/25))/(1 - \exp(-V/25))) \quad (4)$$

The resulting relative P_{K} values for the membrane's permeability to K^+ were fitted with a first-order Boltzmann function or, for coexpression of wild-type and Gly469Arg KCNH1 channel subunits, with the sum of two first-order Boltzmann functions analogous to equation (3)

$$P_{\mathrm{K}}/P_{\mathrm{K,max}} = a/(1 + \exp(-(V - V_{a;0.5})/k_a)) + b/(1 + \exp(-(V - V_{b;0.5})/k_b)) + c \quad (5)$$

Fit results to whole-cell conductance data and permeability data are given in **Supplementary Table 4**.

Statistics. Experimental data are given as means ± s.e.m., with n representing the number of experiments from different cells. One-way ANOVA with *post-hoc* Bonferroni t test or Student's two-tailed unpaired t test (homoscedastic where not otherwise stated) was used to test for significance as indicated with $\alpha = 0.05$.

52. Li, H. & Durbin, R. Fast and accurate short read alignment with Burrows-Wheeler transform. *Bioinformatics* **25**, 1754–1760 (2009).
53. McKenna, A. *et al.* The Genome Analysis Toolkit: a MapReduce framework for analyzing next-generation DNA sequencing data. *Genome Res.* **20**, 1297–1303 (2010).
54. Cingolani, P. *et al.* A program for annotating and predicting the effects of single nucleotide polymorphisms, SnpEff: SNPs in the genome of *Drosophila melanogaster* strain w^{1118}; iso-2; iso-3. *Fly (Austin)* **6**, 80–92 (2012).
55. Liu, X., Jian, X. & Boerwinkle, E. dbNSFP v2.0: a database of human non-synonymous SNVs and their functional predictions and annotations. *Hum. Mutat.* **34**, E2393–E2402 (2013).
56. Kircher, M. *et al.* A general framework for estimating the relative pathogenicity of human genetic variants. *Nat. Genet.* **46**, 310–315 (2014).
57. Biasini, M. *et al.* SWISS-MODEL: modelling protein tertiary and quaternary structure using evolutionary information. *Nucleic Acids Res.* **42**, W252–W258 (2014).
58. Roy, A., Kucukural, A. & Zhang, Y. I-TASSER: a unified platform for automated protein structure and function prediction. *Nat. Protoc.* **5**, 725–738 (2010).
59. Pettersen, E.F. *et al.* UCSF Chimera—a visualization system for exploratory research and analysis. *J. Comput. Chem.* **25**, 1605–1612 (2004).
60. Schuster, A.M., Glassmeier, G. & Bauer, C.K. Strong activation of ether-à-go-go–related gene 1 K^+ channel isoforms by NS1643 in human embryonic kidney 293 and Chinese hamster ovary cells. *Mol. Pharmacol.* **80**, 930–942 (2011).
61. Clay, J.R. Determining K^+ channel activation curves from K^+ channel currents often requires the Goldman-Hodgkin-Katz equation. *Front. Cell. Neurosci.* **3**, 20 (2009).
62. Schönherr, R. *et al.* Individual subunits contribute independently to slow gating of bovine EAG potassium channels. *J. Biol. Chem.* **274**, 5362–5369 (1999).